Postprint of: Winiarski M., Tran T., Chamorro J., Mcqueen T., (CsX)Cu5O2(PO4)2 (X = Cl, Br, I): A Family of Cu2+ S = 1/2 Compounds with Capped-Kagomé Networks Composed of OCu4 Units, INORGANIC CHEMISTRY, Vol. 58, iss. 7 (2019), pp. 4328-4336

$(CsX)Cu_5O_2(PO_4)_2$ (X = Cl, Br, I) – a family of Cu^{2+} S = ½ compounds with capped-kagomé networks composed of OCu_4 units.

Michal J. Winiarski[†‡], Thao T. Tran[†], Juan R. Chamorro[†], Tyrel M. McQueen[†‖*]

† Department of Chemistry, Department of Physics and Astronomy, and Institute for Quantum Matter, Johns Hopkins University, Baltimore, MD, 21218, USA

‡ Faculty of Applied Physics and Mathematics, Gdansk University of Technology, ul. Narutowicza 11/12, 80-233 Gdansk, Poland

‖ Department of Materials Science and Engineering, Johns Hopkins University, Baltimore, MD, 21218, USA

ABSTRACT: Three new salt inclusion compounds $(CsX)Cu_5O_2(PO_4)_2$ (X = Cl, Br, I), phosphate analogues of the kagomé mineral averievite, are reported. Their crystal structures are composed of trigonal networks of corner-sharing OCu_4 anion-centered tetrahedra, forming capped-kagomé planes, which can also be regarded as two-dimensional slices along the [111] direction of a pyrochlore lattice. Magnetization and heat capacity measurements reveal strong geometric frustration of this network and complex magnetic behavior. X-ray and neutron diffraction studies show that all three compounds undergo a trigonal to monoclinic phase transition upon cooling, with a first-order phase transition seen in CsBr and CsI analogs. Along with the previously reported $(CsCl)Cu_5O_2(VO_4)_2$, these three new compounds belong to a large family of OCu_4-based networks which are a playground for studying frustrated quantum magnetism.

KEYWORDS Kagomé network, magnetic frustration, salt-inclusion compounds.

1. Introduction

Geometric magnetic frustration is characterized by the inability of a system to satisfy all of the pairwise interactions and form a single non-degenerate ground state. Frustrated magnetic materials have been intensively studied for their potential to harbor novel and interesting states of matter, such as quantum spin liquids (QSLs) [1], superconductivity [2,3], and topological states [4–6].

Among the frustrated lattices, the kagomé network has been one of the most well studied [1,7,8]. Arrangement of magnetic ions on this corner-sharing network of equilateral triangles give rise to a degenerate ground state. A number of perfect and distorted kagomé QSL candidates have been reported, including synthetic analogues of minerals such as herbertsmithite [9–12], barlowite [13], vesigneite [14,15], and volborthite [16].

While crystal structures of inorganic compounds are commonly described as extended arrays of cation-centered coordination polyhedra, some of the crystal structures can be better understood in terms of networks of anion-centered polyhedra [17–19]. This concept was first applied to a mineral dolerophanite, $Cu_2O(SO_4)$, in which there are four inequivalent oxygen sites, three of which belong to the sulfate group, SO_4^{2-}. The fourth, "additional" oxygen is bound directly to four Cu atoms, forming a $(OCu_4)^{6+}$ tetrahedral polycation [20,21]. A number of crystal structures consisting of anion-centered polyhedra were identified subsequently, many belonging to a group of fumarolic minerals found around volcanic fissures [17,18]. It was speculated that the OCu_4 tetrahedra play an important role in transporting copper in volcanic gases, which would explain the abundance of OCu_4-containing minerals around volcanoes such as Izalco (El Salvador), Vesuvius (Italy), or Tolbachik (Russian Federation). This speculation has been supported by chemical transport experiments [18]. OCu_4 units appear also in metal-organic compounds (known there as $Cu_4(\mu_4\text{-}O)$ clusters) [22].

The OCu_4-based extended structures are interesting from the point of view of magnetic properties. The tetrahedral geometry introduces geometric frustration, as interactions within the OCu_4 are antiferromagnetic (AFM) [22,23]. This can result in exotic magnetic ground states, depending strongly on the connectivity of the units, and the details of magnetic interactions. Averievite, $Cu_5O_2(VO_4)_2 \cdot nMCl$ (M = Rb, Cs, Cu^+), is a fumarolic salt-inclusion mineral found on the Main Tolbachik Fracture Eruption among other exhalation products rich in copper halides and pentavalent vanadium oxides [24,25]. The crystal structure of averievite family of materials (Fig. 1(a)) consist of capped-kagomé layers, composed of corner-sharing OCu_4 units arranged in an up-down-up-down manner (see Fig. 1(b,c)). There are two non-equivalent Cu^{2+} sites in the structure: one forming kagomé layers – Cu1, and one forming two triangular networks that cap the kagomé planes. Cu1 atoms have an effectively square planar coordination with 4 O^{2-} anions, with two apical Cl^- ions positioned at a relatively large distance, while Cu2 sits in a distorted CuO_5 trigonal bipyramid.

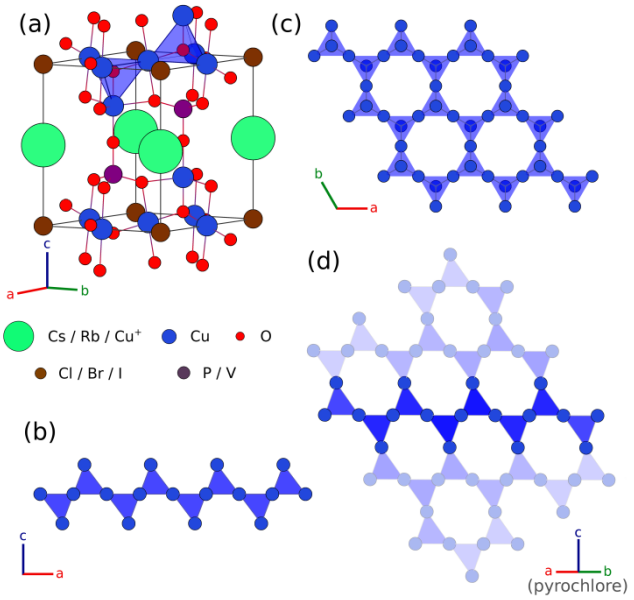

Figure 1. Crystal structure of averievite analogues. Panel (a) shows the unit cell, consisting of OCu_4-PO_4 framework with characteristic channels filled by Cs/Rb/Cu^+ and halide ions. Edge sharing OCu_4 tetrahedra, form a capped-kagomé network shown in panels (b) and (c). The capped-kagomé layer can also be viewed as a two-dimensional slab cut from a pyrochlore lattice (d).

Diamagnetic VO_4/PO_4 tetrahedra separate these layers, isolating them from each other, resulting in prevalently 2D magnetic interactions within the *ab* plane. There are three inequivalent oxygen positions, two of them forming vanadate groups, and one (O2) exclusively bound to four Cu atoms of OCu_4 units. The interlinked OCu_4 and VO_4/PO_4 tetrahedra form an electroneutral, 3D network with separated, infinite channels along the *c* direction, which are occupied by M^+ and Cl^- ions. While the Cu^{2+} ions forming the "capped-kagomé" framework have one unpaired electron ($3d^9$ configuration, S = ½), the Cu^+ cations that occupy the channels are nonmagnetic ($3d^{10}$, S = 0).

The synthetic analogue of averievite, $(CsCl)Cu_5O_2(VO_4)_2$, was recently synthesized and studied [26,27]. X-ray diffraction measurements have shown that the compound undergoes a structural phase transition to monoclinic symmetry just above room temperature (T ≈ 310 K) and a second transition at T = 127 K, which may involve ordering of the Cs sublattice, which was found to be disordered at room temperature [27]. A theoretical study of the magnetic interactions in averievite by Volkova and Marinin [23] has shown antiferromagnetic interactions within the OCu_4 units, with a majority of the net AFM interaction arising from superexchange through the O2 atom.

In this work we report a successful synthesis of three new phosphate analogues of averievite $(CsX)Cu_5O_2(PO_4)_2$ (*X* = Cl, Br, I) and describe their crystal structures and magnetic properties. Despite the similarities between phosphate and vanadate groups, properties of the three new materials are different than those of vanadate analogue.

2. Experimental section

Polycrystalline samples of $(CsX)Cu_5O_2(PO_4)_2$ were synthesized by a solid-state reaction of cesium halides with the $Cu_5O_2(PO_4)_2$. The $Cu_5O_2(PO_4)_2$ precursor was prepared by reacting stoichiometric amounts of ammonium dihydrogen phosphate, $NH_4H_2PO_4$ (Amresco, ACS grade), and copper(II) oxide (Bean Town Chemicals, 99.995% pure). Reagents were finely-ground in an agate mortar, pressed into pellets, and pre-reacted in air at 500°C in order to decompose $NH_4H_2PO_4$ but prevent possible evaporative loss of P_2O_5. Pre-reacted soft pellets were ground, re-pressed, and subsequently sintered in air at 750°C, 850°C, and 880°C with intermediate re-grindings. The x-ray diffraction (XRD) pattern of as-obtained powder matched the reported crystal structure of $Cu_5O_2(PO_4)_2$ [28,29]. As-obtained $Cu_5O_2(PO_4)_2$ powder was mixed and ground with Cs*X* (*X* = Cl, Br, I; all Alfa Aesar, 99.9%, 99%, 99.9%, respectively), pelletized, sealed in evacuated silica glass tubes re-filled with Ar gas, and reacted at 550-580°C with multiple intermediate re-grinding steps. Progress of the reaction was monitored by means of powder XRD and the number of re-grinding steps and annealing times was adjusted to yield phase-pure samples. While Cl- and Br-bearing samples were quenched in air, the I-analogue required furnace-cooling in order to allow iodine vapors to equilibrate with the sample.

All the reagents were used as obtained, without additional purification. Cesium halides were kept in an Ar-filled glovebox to protect them from moisture and oxidation of Br^- and I^-.

An attempt to synthesize $(CsCl)Cu_3Mg_2O_2(PO_4)_2$ with Mg^{2+} substitution at the Cu2 site was unsuccessful as the hypothesized precursor compound $Cu_3Mg_2O_2(PO_4)_2$ could not be obtained.

Synchrotron XRD patterns of $(CsCl)Cu_5O_2(PO_4)_2$ were collected using the 11-BM beamline at Advanced Photon Source, Argonne National Laboratory. Patterns were collected at T = 295 K and T = 100 K. Time-of-flight neutron diffraction (ToF ND) patterns were collected at T = 300 K, T = 100 K , and T = 10 K on the POWGEN instrument of Spallation Neutron Source at Argonne National Laboratory (with detector banks no. 1 and 3). Structures of CsBr and CsI analogues were studied using a laboratory-based Bruker D8 Focus dffractometer with CuK_α radiation. Low-temperature XRD patterns were collected on Bruker D8 Advance with an Oxford Cryosystem PheniX cryocontroller. All ND and XRD patterns were analyzed by means of Rietveld refinement using the FullProf software package [30]. In case of neutron patterns it was found that the stability and quality (defined as the overall match of the calculated profile to the experimental one, rather than just the values of *R* factors) of refinement was significantly improved by applying a maximal likelihood weighting scheme [31] instead of standard least-squares method.

Magnetization measurements on powdered samples were done with the ACMS option of Quantum Design Physical Properties Measurement System (PPMS) using the standard polyethylene straw sample holders. Magnetic susceptibility was approximated as magnetization divided by the applied magnetic field: $\chi \approx M/H$. Heat capacity was measured using the PPMS, employing the semi-adiabatic pulse technique.

Diffuse reflectance spectra of the three compounds and the $Cu_5O_2(PO_4)_2$ precursor were measured using an Agilent Cary 5000 UV-Vis-NIR spectrometer.

VESTA software was used for visualization of crystal structures and geometrical calculations [32]. Bond valence calculations were performed using the BondStr program of the FullProf package [30]. Models of distorted structures were produced using the PowderCell 2.4 program [33].

3. Results and discussion

Samples of Cl-, Br-, and I-bearing compounds are olive-green, yellow-green, and yellow-brown, respectively, all distinct from the deep green color of the $Cu_5O_2(PO_4)_2$ precursor (see Fig. 2(a)). The visible light absorption spectra of (Cs*X*)$Cu_5O_2(PO_4)_2$ and $Cu_5O_2(PO_4)_2$ are shown in Fig. 2(b). The latter compound shows a single, almost completely symmetric absorption minimum centered at ca. 540 nm. In the three (Cs*X*)$Cu_5O_2(PO_4)_2$ compounds the absorption edge is systematically red-shifted with decreasing ligand strength in Cl – Br – I series. This suggests that the transition involves 3*d* orbitals of Cu1, as halide ions does not contribute directly to the coordination of Cu2. The overall shape of the absorption spectrum is more complicated than in the precursor compound. The relatively small shift of absorption edge (~20 nm) along with reduced absorption in the NIR region results in a rather vivid change in color (yellow-green to brown) due to the sensitivity of human eye in that wavelength range, as it can be seen in the CIE 1931 diagram (see Fig. S1 of Supplementary Material).

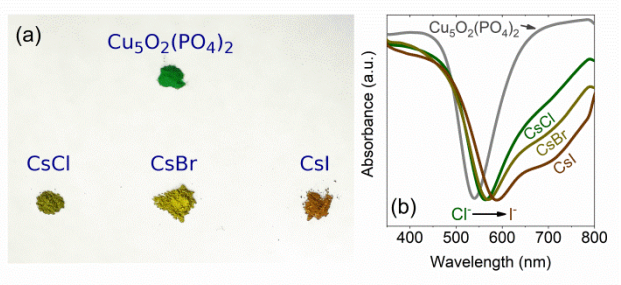

Figure 2 (a) Powders of $Cu_5O_2(PO_4)_2$ and (Cs*X*)$Cu_5O_2(PO_4)_2$, *X* = Cl, Br, I, showing distinct colors. (b) Relative absorbance of the four materials in the visible light region. The absorption edge of (Cs*X*)$Cu_5O_2(PO_4)_2$ shifts by about 20 nm with the decreasing ligand strength from Cl^- to I^-.

The stability of (CsCl)$Cu_5O_2(PO_4)_2$ and (CsBr)$Cu_5O_2(PO_4)_2$ in water was tested by stirring ~2 mg of powdered samples with 20 ml of deionized water in a closed vial at room temperature.. The XRD pattern of the CsCl sample exposed to water for approx. 18 hours shows a significant amount of $Cu_5O_2(PO_4)_2$, which suggests that deintercalation of Cs^+ and Cl^- ions results in a collapse of the trigonal structure, in line with the previous suggestions of the possible ion mobility [18]. In contrast, the CsBr sample did not shown observable amounts of $Cu_5O_2(PO_4)_2$ even after 5 days of stirring. Thissuggests lower mobility of ionic species in the compound, compared to the CsCl variant.

Crystal structure

The room temperature XRD and ND pattern of (Cs*X*)$Cu_5O_2(PO_4)_2$ are successfully fit with a trigonal model (space group *P*-3*m*1, no. 164), as shown in Fig. 3 (XRD) and Fig. S2 of Supplementary Material (ND).

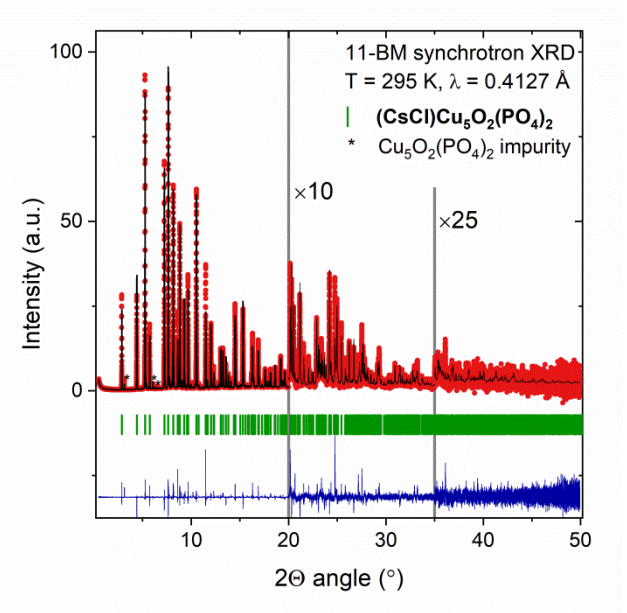

Figure 3 Rietveld fit (black line) to high-resolution synchrotron XRD pattern of (CsCl)$Cu_5O_2(PO_4)_2$ collected at T = 295 K (red points). Green tick marks expected positions of Bragg reflections for the main phase. $Cu_5O_2(PO_4)_2$ impurity reflections are marked with an asterisk.

Details of the crystal structure model of (CsCl)$Cu_5O_2(PO_4)_2$ derived from a Rietveld fit to high-resolution synchrotron XRD are given in Tab. 1. The fit to the ND pattern fit yielded a consistent result and a small differences in unit cell parameters can be attributed to a greater uncertainty of absolute peak positions in ToF ND neutron diffractometer. ND patterns and refinement results are presented in Supplementary Material, Tab. S1. Trace of unreacted CsCl and $Cu_5O_2(PO_4)_2$ (~4 and 5 mol.%, respectively). were accounted for in the refinement. Compared to the reported structure of synthetic averievite, (CsCl)$Cu_5O_2(VO_4)_2$, the unit cell volume of (CsCl)$Cu_5O_2(PO_4)_2$ is about 8% smaller, in agreement with relative sizes of the vanadate and phosphate groups (volume of the tetrahedron 2.4 $Å^3$ vs. 1.8 $Å^3$, respectively). We have found that introduction of Cs site disorder into the structural model results in a significant improvement of refinements, similar to what was reported for (CsCl)$Cu_5O_2(VO_4)_2$ by Botana *et al.* [27]. Mapping of the bond-valence sum (BVS) for Cs^+ ion in the unit cell supports the disordered model, showing that Cs atoms sit in a double well-type potential within voids of the electroneutral copper oxyphosphate framework (See Fig. 4).

Laboratory powder XRD patterns showed that a pure (CsBr)$Cu_5O_2(PO_4)_2$ compound was obtained with no observable crystalline impurity peaks. In case of the CsI analogue a trace amount of unrecognized crystalline impurity was observed. Microstrain and grain size analysis was done, using high purity silicon as an instrumental broadening standard, but, in both compounds the broadening was found to be below the instrument resolution limit. Details of the crystal structures for the CsBr and CsI compounds are presented in Table S2 and Table S3 of the Supplementary Material along with XRD (Fig. S3 and Fig. S4).

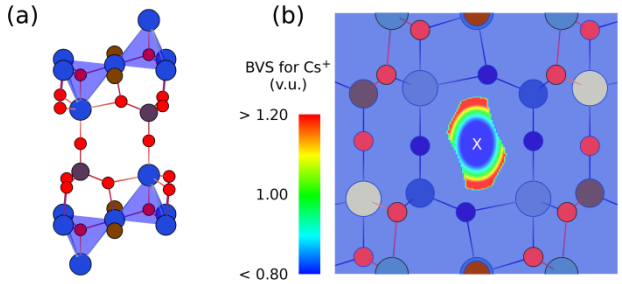

Figure 4 (a) The copper oxyphosphate framework of (Cs*X*)$Cu_5O_2(PO_4)_2$. (b) Map of the bond valence sum (BVS; given in valence units – v.u.) calculated for Cs^+ cation within the unit cell. White X symbol marks the idealized (0,0, ½) position, at which the deviation between BVS and the actual valence is larger than 20%. The lowest deviation (and therefore a potential energy minimum [34]) is found off the idealized position, which is in line with the double-well site potential and observed disorder. Calculations were done using the *softBV* set of parameters [35].

Chemical formula: (CsCl)$Cu_5O_2(PO_4)_2$	
Source	synchrotron
Formula weight (g/mol)	708.03
Temperature (K)	295
Wavelength (Å)	0.4127
Crystal system	trigonal
Space group	P -3 m 1 (no. 164)
$a = b$ (Å)	6.19278(1)
c (Å)	8.24802(1)
$\alpha = \beta$ (°)	90
γ (°)	120
V (Å^3)	273.938
Z	1
ρ_{calc} (g/cm^3)	4.29
d-space range (Å)	0.5 – 47
χ^2	6.69
R-factors (%)	R_p = 14.9, R_{wp} = 16.7, R_{exp} = 6.45

Atomic positions:

	x	y	z	B (Å^2)
Cs (s.o.f. = ½)	0	0	0.5369(1)	2.42(2)
Cu1	⅓	⅔	0.2879(1)	0.69(2)
Cu2	½	½	0	1.55(1)
P	⅓	⅔	0.6900(2)	0.73(3)
Cl	0	0	0	1.62(4)
O1	⅓	⅔	0.5111(6)	0.72(6)
O2	⅓	⅔	0.0661(4)	0.24(6)
O3	0.5300(2)	0.4700(2)	0.2371(2)	2.20(5)

Table 1. Unit cell parameters and atomic coordinates for (CsCl)$Cu_5O_2(PO_4)_2$ at T = 295 K as obtained from Rietveld fit to a high-resolution synchrotron XRD pattern. The disordered Cs site is assumed to be half-occupied, and the s.o.f. was set to ½ and not refined. Conventional background-corrected Rietveld R factors for the fit calculated only for points with Bragg contributions [36,37]. For the definition of R-factors see the Supplementary Material.

In all three compounds the BVS for O2 is substantially larger than 2 (2.46(1), 2.44(1), and 2.31(1) for chloride, bromide, and iodide analogues, respectively), suggesting strong bonding and confirming that the OCu_4 unit is the basic building block of the structure. BVS values for the remaining atoms are consistent with assumed valency (+2 for Cu, +5 for P, -2 for O).

Crystal structures of (Cs*X*)$Cu_5O_2(PO_4)_2$ and the precursor compound $Cu_5O_2(PO_4)_2$ share similar features including the presence of OCu_4 tetrahedra and two types of Cu^{2+} coordination. This structural similarity allows us to synthesize (Cs*X*)$Cu_5O_2(PO_4)_2$ at relatively low temperatures by diffusion of Cs^+ and halide ions into the framework. It should be noted, however, that the two structures differ significantly when the connectivity of OCu_4 units is considered – in averievite-type phases they form vertex-sharing capped-kagomé layers interlinked by phosphate groups, while in $Cu_5O_2(PO_4)_2$ they are arranged into infinite one dimensional chains composed of corner sharing O_2Cu_7 dimers (formed by two edge-sharing OCu_4 units). The two networks are related by a shear transformation applied to every other pair of corner-sharing OCu_4 units (see Fig. S2 in Supplementary Material).

Low-temperature XRD (LT-XRD) measurements revealed that CsBr and CsI undergo structural phase transitions at approximately T = 75 K and T = 230 K, respectively, as evidenced by the splitting of reflections below the transition temperatures. These transition temperatures are in agreement with drops in magnetization and heat capacity anomalies (see below). Fig. 5 (a) presents XRD patterns of the CsBr analogue between T = 40 and T = 100 K, showing a structural phase transition around T = 75 K. An analogous splitting of the 102 reflection was observed in CsI analogue around T = 230 K (Fig. 5(b). Both CsBr and CsI compounds show a discontinuous lattice contraction along the c direction upon cooling below the structural phase transition temperature as it is highlighted by the shift of (002) peak in Fig. 5(b).

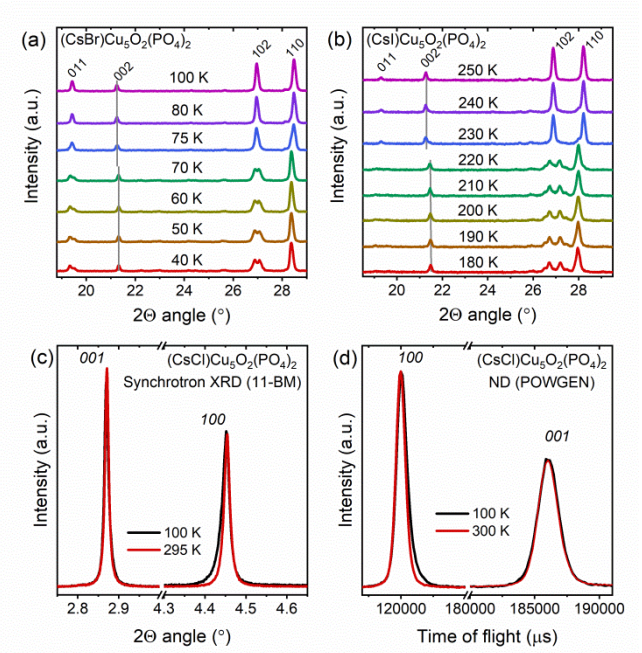

Figure 5 Panels (a) and (b) show low-temperature XRD patterns of (CsBr)$Cu_5O_2(PO_4)_2$ and (CsI)$Cu_5O_2(PO_4)_2$, respectively, with peak

splitting due to phase transition seen around T = 70-75 K and T = 220-230 K. A sudden decrease of the *c* parameter is also seen upon the transition, which is highlighted by two gray lines in panel (b). Panels (c) and (d) show synchrotron XRD and ND patterns, respectively, collected at room temperature and 100 K. A significant asymmetry of 100 peak is seen at 100 K, while 001 reflection remain symmetric.

In the case of CsCl, the LT-XRD pattern collected at 12 K shows a distinct splitting of reflections, but a significant peak asymmetry is seen at 100 K (see Fig. S6 of Supplementary Material). A magnetic transition and heat capacity anomaly are seen around 12 K in the CsCl analogue, but its structural origin is not certain (see below). It is possible that in the case of the CsCl compound, the structural distortion develops gradually over a range of temperatures and has the character of a phase crossover rather than a true structural transition. For clarity of the discussion we will, however, assume that 12 K is thetemperature of a structural transition.

In all three compounds the structural transition temperature is lower than that observed for $(CsCl)Cu_5O_2(VO_4)_2$ (T = 310 K). The large difference between transition temperatures of $(CsCl)Cu_5O_2(VO_4)_2$ and its phosphate analogues (T = 310 K vs. T = 75 K and T = 230 K, for $(CsBr)Cu_5O_2(PO_4)_2$ and $(CsI)Cu_5O_2(PO_4)_2$, respectively) can likely be attributed to a positive chemical pressure applied by the substitution of VO_4 by significantly smaller PO_4 that acts to stabilize the trigonal symmetry. Meanwhile, the substitution of Cl^- by much larger Br^- and I^- acts as negative pressure, resulting in a shift of the structural phase transition back to the higher temperature range.

Synchrotron XRD and ND data of $(CsCl)Cu_5O_2(PO_4)_2$ at T = 100 K show a significant asymmetry of (*h k l*), $h, k \neq 0$ reflections, with (0 0 *l*) reflections remaining nearly symmetric, as shown in Fig. 5(c,d). This suggest that a local structure distortion is present already at T = 100 K, much above the suspected structural transition at T = 12 K. A similar effect was previously observed in PdTeI [38] and the temperature dependent diffraction data reported for $(CsCl)Cu_5O_2(VO_4)_2$ [27] also suggest some deviations from trigonal symmetry before the actual transition. This strong, *hkl*-dependent asymmetry could not be modelled using the peak shape functions available in the FullProf program. To allow for Rietveld fit of peak intensities, the synchrotron XRD diffraction pattern was first conditioned using the Savitzky-Golay filter [39] with 5th degree polynomial and window size of 11 data points, and then re-binned by trapezoidal rule integration with the same window size, as implemented in Python 3.6.5 with SciPy 1.1.0 and NumPy 1.14.3 packages [40,41]. The fit to re-binned data is presented in Supplementary Material Fig. S7. Our comparison of the synchrotron XRD patterns collected at T = 100 K and T = 295 K suggests that the relative change of the *a* unit cell parameter is one order of magnitude larger than that of the *c* parameter. This yields a rough estimate of the thermal expansion coefficients $\alpha_a = 5 \cdot 10^{-5}$ K^{-1} and $\alpha_c = 0.5 \cdot 10^{-5}$ K^{-1}, highlighting the stronger bonding along the *c* direction.

The neutron diffraction data of the CsCl compound at T = 10 K (Fig. S8 of Supplementary Material) shows significant reflection splitting consistent with with a trigonal to monoclinic phase transition. However, the pattern could not be successfully fitted with only a monoclinic $P2_1/c$ structure only The refinement was possible only when a mixture of trigonal and monoclinic phases was used. Since the measurement was done at T = 10 K, which is just 2 K below the suspected transition temperature, an incomplete transition is likely. Refinement yields approximately a 3:5 proportion of monoclinic and trigonal phases. Results of the refinement are shown in Tab. S5 of Supplementary Material. Structural origin of the phase transition is evidenced by the results of low-temperature XRD measurements (Fig. S6 of Supplementary Material).

Two weak reflections corresponding to *d*-spacings of 5.05 Å and 5.75 Å are observed at T = 10 K that are not present at T = 100 K (Fig. S8(b) in Supplementary Material). These could not be indexed with either the trigonal or monoclinic cell or ascribed to the nuclear structures of the impurity phases. These reflections may indicate a magnetic order in the material, as the shortest and second-shortest distance between the Cu2 ("capping") atoms is approx. 5 and 6 Å, respectively. However, the combination of the incomplete transition and the scarce number of these reflections precludes the unique identification of their origin. It is unlikely that these reflections arise from the magnetic ordering of the AFM impurity phase $Cu_5O_2(PO_4)_2$ as the small magnetic moment of Cu^{2+} and minute amount present in the sample would not produce observable magnetic reflections.

Magnetization

In all three compounds the structural phase transition is reflected as a discontinuity on the magnetic susceptibility (χ) curves (see Fig. 6(a-c)). Interestingly, the CsBr and CsI compounds show a pronounced thermal hysteresis across the transition, while no hysteresis is observed in CsCl analogue. An antiferromagnetic (AFM) or spin glass-like kink is observed at T_t = 3.8 K, 7.0 K, and 12.5 K for the Cl-, Br-, and I-bearing compound.

Magnetic susceptibility curves above and below the structural transition were fit to the Curie-Weiss relation:

$$\chi(T) = \frac{C}{T - \Theta_{CW}} + \chi_0$$

Where C is the Curie constant, Θ_{CW} is the Curie-Weiss temperature, and χ_0 is a temperature-independent contribution to susceptibility, that includes both electron core diamagnetism of the sample and small diamagnetic signal of the sample holder. The Curie constant C was used to estimate the effective magnetic moment per Cu^{2+} ion using the relation: $\mu_{eff} = \sqrt{\frac{3k_B}{N_A}C}$. Tab. 2 summarizes the results of fits and transition temperatures estimated from magnetic susceptibility. The effective magnetic moment for the CsCl compound is very close to the spin-½ moment of 1.73 μ_B, expected for a $3d^9$ ion with completely quenched orbital moment, while for CsBr and CsI, the values are slightly larger, but still within the limits of values experimentally observed for Cu^{2+}.

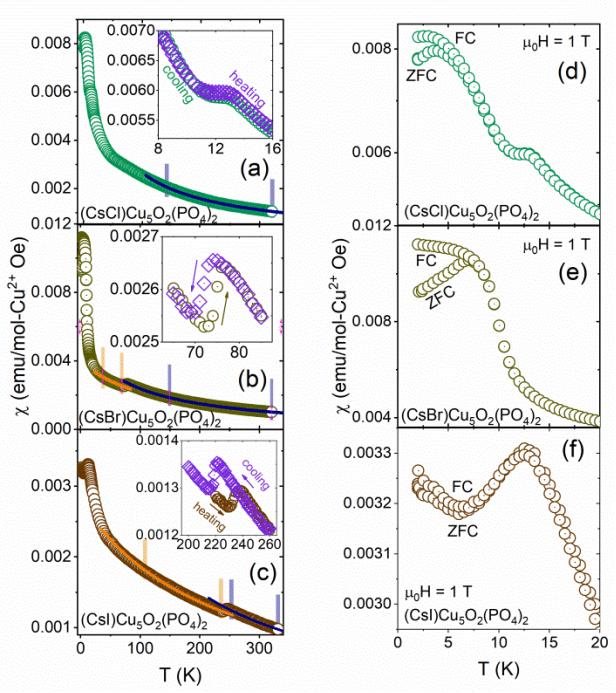

Figure 6 (a,b,c): temperature dependence of magnetic susceptibility of (Cs*X*)$Cu_5O_2(PO_4)_2$ from T = 2 K to 320 K. Solid blue and yellow lines show Curie-Weiss law fits above and below the structural phase transition temperature, respectively. Vertical ticks mark the data range taken for fitting. Insets show thermal hysteresis behavior around the structural transition temperature observed for the bromide and iodide analogues (b,c), but not for (CsCl)$Cu_5O_2(PO_4)_2$ (a). (d,e,f): magnetic susceptibility in the vicinity of magnetic transition.

In addition, magnetic susceptibility of the $Cu_5O_2(PO_4)_2$ precursor powder was measured. The compound shows a pronounced AFM transition at T = 12.7 K (see Fig. S9 of Supplementary Material). Temperature dependence of susceptibility could not be modelled with the Curie-Weiss relation in the studied temperature range.

X in (Cs*X*)$Cu_5O_2(PO_4)_2$ =		Cl	Br	I
Magnetic transition temp., T_t (K)		3.8	7.0	12.5
Structural transition temperature, T_{dist} (K)		12	75	230
High temperature $> T_{dist}$	C (emu K $mol^{-1}Oe^{-1}$)	0.394(7)	0.468(4)	0.571(2)
	μ_{eff} (μ_B)	1.78(2)	1.93(1)	2.14(1)
	Θ_{CW} (K)	-48(2)	-85(1)	-119(2)
	f	13	12	9.5
Low temperature $< T_{dist}$	C (emu K $mol^{-1}Oe^{-1}$)		0.532(8)	0.715(2)
	μ_{eff} (μ_B)		2.06(2)	2.39(1)
	Θ_{CW} (K)		-128(3)	-231(2)
	f		18	18

Table 2 Transition temperatures and Curie-Weiss (C-W) fit parameters for (CsX)$Cu_5O_2(PO_4)_2$. Magnetic transition temperature is defined as the position of maximum of ZFC susceptibility curve at μ_0H = 1 T. *P*-3*m*1 to $P2_1/c$ transition are taken from heating curves. Curie constants *C* are given per mole of Cu^{2+} ions.

Heat capacity

Low-temperature heat capacity of (Cs*X*)$Cu_5O_2(PO_4)_2$ is shown in Fig. 7. In the CsCl compound (Fig. 7(a) and Fig. S10(a) of Supplementary Material) a single small anomaly is observed at ca. 12 K, which is the approximate temperature of the structural phase transition in this material (see Fig. 6 (a)). The peak at T ≈ 12 K seems to broaden slightly under the application of external magnetic field of μ_0H = 3 T, possibly indicative of the magnetic contribution to the specific heat at that transition. Since the $Cu_5O_2(PO_4)_2$ impurity phase has a Néel temperature T_N = 12.7 K, we cannot exclude the possibility that the anomaly can be ascribed to the AFM transition of the impurity phase. This is however less likely than the intrinsic character of the anomaly, due to the small amount of $Cu_5O_2(PO_4)_2$ present in the sample.

In the case of (CsBr)$Cu_5O_2(PO_4)_2$, two peaks are observed on the heat capacity, at T = 9 K and T = 73 K, respectively (see Fig. 7(b) and Fig. S10(b) of Supplementary Material). The latter is due to structural phase transition which is clearly observed in the diffraction data. The former one is suppressed by applied magnetic field, as expected for an AFM or spin glass. Lack of suitable nonmagnetic analogue, which could be used for subtraction of phonon contribution, makes the reliable extraction of magnetic heat capacity and entropy difficult.

In the case of (CsI)$Cu_5O_2(PO_4)_2$, three anomalies are observed (see Fig. 6(f)). At *T* = 230 K a peak due to the structural phase transition is observed (see Fig. S10(d) of Supplementary Material). At *T* = 13 K, a peak corresponding to a possible magnetic order is also observed. There is also a third, unidentified broad peak at *T* = 20 K. All three anomalies remain robust against applied magnetic fields.

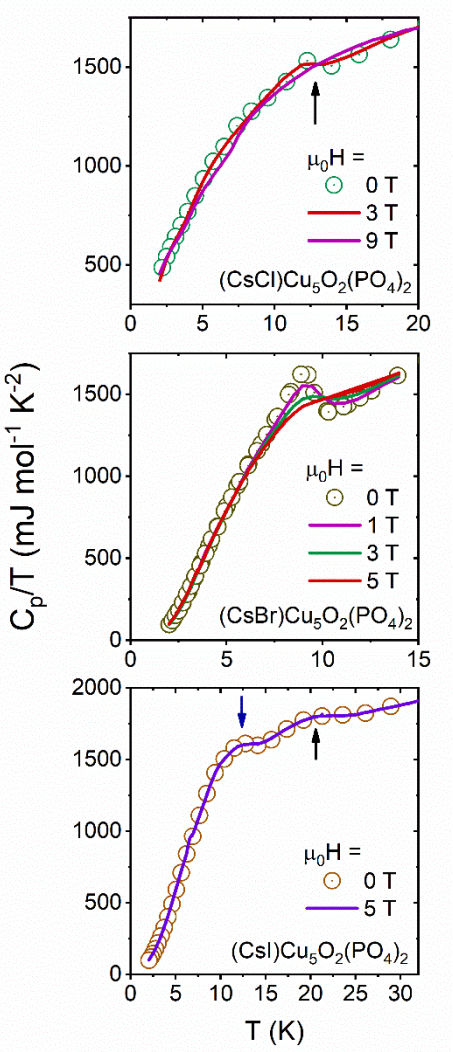

Figure 7 Low temperature heat capacity of (Cs*X*)$Cu_5O_2(PO_4)_2$. For heat capacity results measured between T = 2 K and 300 K see Fig. S10 of Supplementary Material.

Discussion

$(CsCl)Cu_5O_2(PO_4)_2$ was found to be significantly different from its previously-known vanadate counterpart $(CsCl)Cu_5O_2(VO_4)_2$. The major factor responsible for this difference is likely a "chemical pressure" resulting from a much smaller size of PO_4^{3-} unit compared to VO_4^{3-} (note that ionic radius of P^{5+} is over 2 times smaller than V^{5+}, 0.17 Å and 0.36 Å in tetrahedral coordination, respectively [42]). This "chemical pressure" effect would also explain the differences between structural transition temperatures within the (Cs*X*)$Cu_5O_2(PO_4)_2$ family, as substitution of Cl^- with larger Br^- and I^- acts as a negative pressure, partially relieving the compression induced by the phosphate group.

Recent results on Sr_2BOsO_6 double perovskites (*B* = Sc, Y, In) have highlighted the role of closed-shell (d^{10}) vs. open-shell (d^0) configurations of the nonmagnetic cations in determining the magnetic exchange interactions. The magnetic exchange interaction were stronger in case of d^0 systems [43,44]. Taking this into account, it would be interesting to synthesize and study an arsenate analogue of averievite. With a d^{10} As^{5+} anion the coupling between OCu_4 layers should be decreased in strength, leading to more two-dimensional magnetic properties. Arsenate and vanadate anions show very similar sizes (ionic radii of As is 0.34 Å [42]) and chemical properties, and a number of mixed AsO_4-VO_4 systems is known, including the recently reported fumarolic mineral aleutite $[Cu_5O_2](AsO_4)(VO_4)\cdot(Cu,K,Pb,Rb,Cs)Cl$, a structural analogue of averievite [45].

The significant differences in the magnetic properties observed within the group of phosphate averevites (Cs*X*)$Cu_5O_2(PO_4)_2$ (*X* = Cl, Br, I) can likely be explained by the effects of the halide ion on the structure of the OCu_4 network. It is known that the strength and sign of superexchange interaction in Cu^{2+} oxides depends strongly on the Cu-O-Cu bond angle [46,47]. In our case, this is reflected in the differences of the Curie-Weiss temperature in the series (from -48 K in CsCl compound to -119 K in CsI, see Table 2). Direct comparison of bond angles and distances between all three compounds is difficult due to preferred orientation issues present in the CsCl synchrotron XRD pattern. However, insight into the structures of CsBr and CsI analogues shows that the Cu1-O2-Cu1 (kagomé plane) bond angle increases from 112° to 113°, respectively, while the Cu1-O2-Cu2 angle decreases from 107° to 105°. This should result in a stronger AFM coupling within the kagomé plane and weaker interaction with the "capping" layer. The final change in magnetic properties results from an interplay of exchange interaction between different Cu sites, structural distortion (affected strongly by the "chemical pressure"), and geometric frustration (which is at least partially relieved upon the structural transition).

The detailed magnetic ground states of all three compounds remain unclear. On the one hand, the rather broad kink of magnetization, splitting of ZFC and FC magnetization curves and the presence of small magnetization hysteresis (see Fig. S11(a,b) of the Supplementary Material) in CsCl and CsBr analogues suggest a spin glass transition. On the other hand, a rather sharp heat capacity anomaly at transitions (especially in the CsBr case) and lack of visible change of transition temperature upon change of the excitation frequency in ac magnetization (see Fig. S11(c,d) of the Supplementary Material) suggest an AFM ordering. This would also explain the occurrence of additional peaks in the ND pattern of the CsCl analogue collected at 10 K. Further studies of the magnetic properties of the $(CsCl)Cu_5O_2(PO_4)_2$ would require a sample free of the AFM $Cu_5O_2(PO_4)_2$ impurity, preferably in the form of a single crystal.

Conclusions

We have successfully synthesized a series of three phosphate analogues of the mineral averievite, with a frustrated "capped kagomé" lattice of Cu^{2+} ions. XRD and ND patterns suggest that all three compounds undergo a structural phase transition from trigonal to monoclinic symmetry upon cooling. The temperature of the transition depends strongly on the halide ion, ranging from 12 K to 230 K in case of Cl and I, respectively.

Magnetic properties of all three compounds show effects of strong geometrical frustration. In spite of the structural similarity each of the systems show distinct magnetic behavior. It may be possible to further tune the magnetic ground state may by

exchanging the phosphate anion to vanadate and possibly arsenate. This feature makes the averievite family of compounds an interesting tunable system for studying the magnetic properties of frustrated systems. In a broader view, the averievite family is only one of the members of a vast group of compounds based on OCu_4 units showing various types of connectivity and dimensionality [17–19].

ASSOCIATED CONTENT

Supporting Information. Supplementary Material presenting XRD and ND patterns and crystallographic data of described compounds; magnetization results for $Cu_5O_2(PO_4)_2$ and additional heat capacity plots This material is available free of charge via the Internet at http://pubs.acs.org.

AUTHOR INFORMATION

Corresponding Author

* mcqueen@jhu.edu

Author Contributions

The manuscript was written through contributions of all authors.

ACKNOWLEDGMENT

This work was supported as part of the Institute for the Quantum Matter, an Energy Frontier Research Center funded by the US Department of Energy, Office of Science, Office of Basic Energy Sciences, under award DE-SC0019331.
Use of the Advanced Photon Source at Argonne National Laboratory was supported by the US Department of Energy, Office of Science, Office of Basic Energy Sciences, under Contract No. DE-AC02-06CH11357.
The research at Oak Ridge National Laboratory's Spallation Neutron Source was sponsored by the US Department of Energy, Office of Basic Energy Sciences, Scientific User Facilities Division.
We would like to thank prof. Susanna Thon and Yida Lin for the help with spectroscopic measurements.

ABBREVIATIONS

AFM – antiferromagnet/antiferromagnetic; ND – neutron diffraction; XRD – x-ray diffraction.

REFERENCES

(1) Balents, L. Condensed-Matter Physics: Quantum Mechanics in a Spin. *Nature* **2016**, *540*, 534–535.
(2) Anderson, P. W. RVB Theory of High Tc Superconductivity. In *Novel Superconductivity*; Springer, Boston, MA, 1987; pp 295–299.
(3) Lee, P. A. From High Temperature Superconductivity to Quantum Spin Liquid: Progress in Strong Correlation Physics. *Rep. Prog. Phys.* **2008**, *71*, 012501.
(4) Zhang, L.; Ren, J.; Wang, J.-S.; Li, B. Topological Magnon Insulator in Insulating Ferromagnet. *Phys. Rev. B* **2013**, *87*, 144101.
(5) Chisnell, R.; Helton, J. S.; Freedman, D. E.; Singh, D. K.; Bewley, R. I.; Nocera, D. G.; Lee, Y. S. Topological Magnon Bands in a Kagome Lattice Ferromagnet. *Phys. Rev. Lett.* **2015**, *115*, 147201.
(6) Wang, C.; Nahum, A.; Senthil, T. Topological Paramagnetism in Frustrated Spin-1 Mott Insulators. *Phys. Rev. B* **2015**, *91*, 195131.
(7) Ramirez, A. P. Strongly Geometrically Frustrated Magnets. *Annu. Rev. Mater. Sci.* **1994**, *24*, 453–480.
(8) Nocera, D. G.; Bartlett, B. M.; Grohol, D.; Papoutsakis, D.; Shores, M. P. Spin Frustration in 2D Kagomé Lattices: A Problem for Inorganic Synthetic Chemistry. *Chem. – Eur. J.* **2004**, *10*, 3850–3859.
(9) Norman, M. R. Colloquium: Herbertsmithite and the Search for the Quantum Spin Liquid. *Rev. Mod. Phys.* **2016**, *88*, 041002.
(10) Colman, R. H.; Sinclair, A.; Wills, A. S. Magnetic and Crystallographic Studies of Mg-Herbertsmithite, γ-Cu3Mg(OH)6Cl2—A New S = 1/2 Kagome Magnet and Candidate Spin Liquid. *Chem. Mater.* **2011**, *23*, 1811–1817.
(11) Han, T.-H.; Helton, J. S.; Chu, S.; Nocera, D. G.; Rodriguez-Rivera, J. A.; Broholm, C.; Lee, Y. S. Fractionalized Excitations in the Spin-Liquid State of a Kagome-Lattice Antiferromagnet. *Nature* **2012**, *492*, 406–410.
(12) Kelly, Z. A.; Gallagher, M. J.; McQueen, T. M. Electron Doping a Kagome Spin Liquid. *Phys. Rev. X* **2016**, *6*, 041007.
(13) Pasco, C. M.; Trump, B. A.; Tran, T. T.; Kelly, Z. A.; Hoffmann, C.; Heinmaa, I.; Stern, R.; McQueen, T. M. Single Crystal Growth of Cu4(OH)6BrF and Universal Behavior in Quantum Spin Liquid Candidates Synthetic Barlowite and Herbertsmithite. *Phys. Rev. Mater.* **2018**, *2,* 044406.
(14) Okamoto, Y.; Yoshida, H.; Hiroi, Z. Vesignieite BaCu3V2O8(OH)2 as a Candidate Spin-1/2 Kagome Antiferromagnet. *J. Phys. Soc. Jpn.* **2009**, *78*, 033701.
(15) Ishikawa, H.; Yajima, T.; Miyake, A.; Tokunaga, M.; Matsuo, A.; Kindo, K.; Hiroi, Z. Topochemical Crystal Transformation from a Distorted to a Nearly Perfect Kagome Cuprate. *Chem. Mater.* **2017**, *29*, 6719–6725.
(16) Bert, F.; Bono, D.; Mendels, P.; Ladieu, F.; Duc, F.; Trombe, J.-C.; Millet, P. Ground State of the Kagome-Like S=1/2 Antiferromagnet Volborthite Cu3V2O7(OH)2·2H2O. *Phys. Rev. Lett.* **2005**, *95*, 087203.
(17) Krivovichev, S. V.; Filatov, S. K.; Semenova, T. F. Types of Cationic Complexes Based on Oxocentred Tetrahedra [OM4] in the Crystal Structures of Inorganic Compounds. *Russ. Chem. Rev.* **1998**, *67*, 137.
(18) Krivovichev, S. V.; Mentré, O.; Siidra, O. I.; Colmont, M.; Filatov, S. K. Anion-Centered Tetrahedra in Inorganic Compounds. *Chem. Rev.* **2013**, *113*, 6459–6535.
(19) Hawthorne, F. C. The Structure Hierarchy Hypothesis. *Mineral. Mag.* **2014**, *78*, 957–1027.
(20) Bergerhoff, G.; Paeslack, J. Sauerstoff Als Koordinationszentrum in Kristallstrukturen. *Z. Für Krist.-Cryst. Mater.* **1968**, *126*, 112–123.
(21) Effenberger, H. Cu2O(SO4), Dolerophanite: Refinement of the Crystal Structure, with a Comparison of [O Cu(II)4] Tetrahedra in Inorganic Compounds. *Monatshefte Für Chem. Chem. Mon.* **1985**, *116*, 927–931.
(22) Shakya, R.; Hindo, S. S.; Wu, L.; Ni, S.; Allard, M.; Heeg, M. J.; da Rocha, S. R. P.; Yee, G. T.; Hratchian, H. P.; Verani, C. N. Amphiphilic and Magnetic Properties of a New Class of Cluster-Bearing [L2Cu4(M4-O)(M2-Carboxylato)4] Soft Materials. *Chem. – Eur. J.* **2007**, *13*, 9948–9956.
(23) Volkova, L. M.; Marinin, D. V. Antiferromagnetic Spin-Frustrated Layers of Corner-Sharing Cu 4 Tetrahedra on the Kagome Lattice in Volcanic Minerals Cu5O2(VO4)2·(CuCl), NaCu5O2(SeO3)2Cl3 , and K2Cu5Cl8(OH)4·2H2O. *J. Phys. Condens. Matter* **2018**, *30*, 425801.
(24) Starova, G. L. The Crystal Structure of Averievite, Cu5O2(VO4)2·nMX: Comparison with Related Compounds. *Mineral. Mag.* **1997**, *61*, 441–446.
(25) Vergasova, L. P.; Filatov, S. K. New Mineral Species in Products of Fumarole Activity of the Great Tolbachik Fissure Eruption. *J. Volcanol. Seismol.* **2012**, *6*, 281–289.
(26) Queen, W. L. Synthesis and characterization of magnetic solids containing periodic arrays of transition metal oxide nanostructures. Ph.D. Thesis, Clemson University, Clemson, SC, United States, 2009.

(27) Botana, A. S.; Zheng, H.; Lapidus, S. H.; Mitchell, J. F.; Norman, M. R. Averievite: A Copper Oxide Kagome Antiferromagnet. *Phys. Rev. B* **2018**, *98*, 054421.
(28) Brunel-Laügt, M.; Guitel, J.-C. Structure Cristalline de Cu5O2(PO4)2. *Acta Crystallogr. Sect. B* **1977**, *33*, 3465–3468.
(29) Grazulis, S.; Chateigner, D.; Downs, R. T.; Yokochi, A. F. T.; Quiros, M.; Lutterotti, L.; Manakova, E.; Butkus, J.; Moeck, P.; Le Bail, A. Crystallography Open Database - an Open-Access Collection of Crystal Structures. *J. Appl. Crystallogr.* **2009**, *42*, 726–729.
(30) Rodríguez-Carvajal, J. Recent Advances in Magnetic Structure Determination by Neutron Powder Diffraction. *Phys. B Condens. Matter* **1993**, *192*, 55–69.
(31) Antoniadis, A.; Berruyer, J.; Filhol, A. Maximum-Likelihood Methods in Powder Diffraction Refinements. *Acta Crystallogr. Sect. A* **1990**, *46*, 692–711.
(32) Momma, K.; Izumi, F. VESTA 3 for Three-Dimensional Visualization of Crystal, Volumetric and Morphology Data. *J. Appl. Crystallogr.* **2011**, *44*, 1272–1276.
(33) Kraus, W.; Nolze, G. POWDER CELL – a Program for the Representation and Manipulation of Crystal Structures and Calculation of the Resulting X-Ray Powder Patterns. *J. Appl. Crystallogr.* **1996**, *29*, 301–303.
(34) Adams, S.; Rao, R. P. Transport Pathways for Mobile Ions in Disordered Solids from the Analysis of Energy-Scaled Bond-Valence Mismatch Landscapes. *Phys. Chem. Chem. Phys.* **2009**, *11*, 3210–3216.
(35) Adams, S. Relationship between Bond Valence and Bond Softness of Alkali Halides and Chalcogenides. *Acta Crystallogr. B* **2001**, *57*, 278–287.
(36) Toby, B. H. R Factors in Rietveld Analysis: How Good Is Good Enough? *Powder Diffr.* **2006**, *21*, 67–70.
(37) Huot, J.; Černý, R. Neutron Powder Diffraction. In *Neutron Scattering and Other Nuclear Techniques for Hydrogen in Materials*; Fritzsche, H., Huot, J., Fruchart, D., Eds.; Neutron Scattering Applications and Techniques; Springer International Publishing, 2016; pp 31–89.
(38) Cottingham, P.; Miller, D. C.; Sheckelton, J. P.; Neilson, J. R.; Feygenson, M.; Huq, A.; McQueen, T. M. Dynamic Charge Disproportionation in the 1D Chain Material PdTeI. *J. Mater. Chem. C* **2014**, *2*, 3238–3246.
(39) Savitzky, A.; Golay, M. J. E. Smoothing and Differentiation of Data by Simplified Least Squares Procedures. *Anal. Chem.* **1964**, *36*, 1627–1639.
(40) Oliphant, T. E. *A Guide to NumPy*; Trelgol Publishing: USA, 2006.
(41) Oliphant, T. E. Python for Scientific Computing. *Comput. Sci. Eng.* **2007**, *9*, 10–20.
(42) Shannon, R. D.; Prewitt, C. T. Effective Ionic Radii in Oxides and Fluorides. *Acta Crystallogr. B* **1969**, *25*, 925–946.
(43) Feng, H. L.; Yamaura, K.; Tjeng, L. H.; Jansen, M. The Role of Nonmagnetic d0 vs. d10 B-Type Cations on the Magnetic Exchange Interactions in Osmium Double Perovskites. *J. Solid State Chem.* **2016**, *243*, 119–123.
(44) Kanungo, S.; Yan, B.; Felser, C.; Jansen, M. Active Role of Nonmagnetic Cations in Magnetic Interactions for Double-Perovskite Sr2BOsO6 (B = Y, In, Sc). *Phys. Rev. B* **2016**, *93*, 161116.
(45) Hålenius, U.; Hatert, F.; Pasero, M.; Mills, S. J. New Minerals and Nomenclature Modifications Approved in 2018. *Mineral. Mag.* **2018**, *82*, 779–785.
(46) Kimura, T.; Sekio, Y.; Nakamura, H.; Siegrist, T.; Ramirez, A. P. Cupric Oxide as an Induced-Multiferroic with High-T_C. *Nat. Mater.* **2008**, *7*, 291–294.
(47) Rocquefelte, X.; Schwarz, K.; Blaha, P. Theoretical Investigation of the Magnetic Exchange Interactions in Copper(II) Oxides under Chemical and Physical Pressures. *Sci. Rep.* **2012**, *2*, 759.

For Table of Contents Only

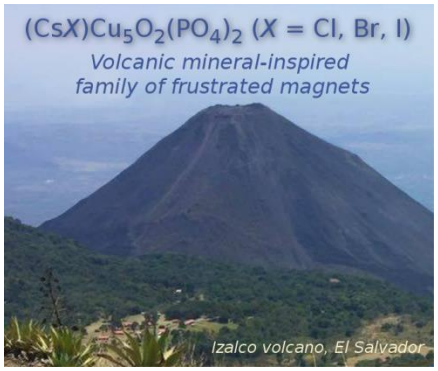

Synopsis: Three new highly frustrated S = 1/2 quantum magnets, (Cs*X*)$Cu_5O_2(PO_4)_2$ (*X* = Cl, Br, I), phosphate analogues of the volcanic kagomé mineral averievite, are reported.